Conference Paper

Multi-component 3-D imaging of ground penetrating radar data using matrix inversion in the spatial Fourier domain

Author(s):
Kruk, Jan van der; Wapenaar, C.P.A.; Fokkema, J.T.

Publication Date:
2000

Permanent Link:

https://doi.org/10.3929/ethz-a-004364145 →

Multi-component 3-D Imaging of ground penetrating radar data using matrix inversion in the spatial Fourier domain,

J. van der Kruk, C.P.A Wapenaar and J.T. Fokkema,*

Proceedings Eight international conference

on

Ground-Penetrating Radar,

Queensland, Australia, May 23-26, 2000, pp. 508-513.

Delft University of Technology,

Faculty of Applied Earth Sciences,

Section of Applied Geophysics

*Now working at:

Institute of geophysics, Swiss Federal Institute of Technology

ETH-Hoenggerberg, CH-8093, Zurich, Switzerland

MULTI-COMPONENT 3-D IMAGING OF GROUND PENETRATING RADAR DATA USING MATRIX INVERSION IN THE SPATIAL FOURIER DOMAIN

J. van der Kruk, C.P.A. Wapenaar, J.T. Fokkema
Section of Applied Geophysics, Faculty of Applied Earthsciences, Delft University of Technology,
Mijnbouwstraat 120, 2628 RX Delft, The Netherlands
J.vanderKruk@ta.tudelft.nl, C.P.A.Wapenaar@ctg.tudelft.nl, J.T.Fokkema@ta.tudelft.nl

ABSTRACT

3D imaging of ground penetrating radar data is a challenging task. Most imaging procedures are based on scalar seismic imaging algorithms. However, for electromagnetic imaging the vectorial character of the emitted field and the radiation characteristics of the source and the receiver play an important role. In this paper a new imaging algorithm is presented, which is dedicated to the electromagnetic case. The vectorial character of the electromagnetic waves is taken into account for a monostatic fixed offset ground penetrating radar (gpr) survey, when the source and receiver are present on a dielectric medium.
The forward model is described by the 3D wave field extrapolator which takes into account the vectorial character of the electromagnetic field. The imaging algorithm is based on an approximate inverse of this 3D wave field extrapolator, which is determined in the spatial Fourier domain. For a homogeneous space and a zero-offset configuration it is feasible to carry out an analytical approximation of the inverse operator. The approximate inverse of a scalar 3D wave field extrapolator is not stable, which motivates the use of a multi-component imaging algorithm.
For two homogeneous halfspaces it is not feasible to carry out a similar analytical approach. However, in numerical sense the same procedure can be carried out, which has the important benefit that also the offset between the source and receiver can be taken into account.
Numerical results are presented for a point scatterer in a homogeneous space, which indicates the spatial resolution which can be obtained. Imaging results of experiments are presented, which take into account the vectorial character of the measured electric field, the offset between the source and receiver and the presence of two homogeneous halfspaces.

Key words: 3D imaging, ground penetrating radar, common offset, halfspace

INTRODUCTION

For electromagnetic imaging the vectorial character of the emitted field plays an important role. However, most of the imaging strategies for gpr data are similar to the (scalar) seismic processing algorithms. A tutorial paper by Berkhout (1981) indicated that three methods of wave field extrapolation are commonly used in seismics, i.e., the Kirchhoff-summation approach, the plane-wave method (k-f method), and the finite-difference technique. These three extrapolation methods can also be used to obtain a migration scheme for gpr data to image the subsurface. Fisher et al. (1992) used reverse-time migration based on the scalar wave equation using a finite-difference scheme and compared the results with Kirchhoff migration. Mast and Johansson (1994) carried out a 3D imaging using multi-frequency diffraction tomography (plane wave method) on experimental data. They also compared the obtained results with 3D synthetic aperture imaging on the same experimental data (Johansson and Mast, 1994) and concluded that the plane wave method resulted in better focussed images. Kirchhoff migration is used by Moran et al. (1998) for 3D monostatic and bistatic imaging of gpr data. In commercial applications it will not be feasible to carry out a 3D bistatic (multi offset) gpr survey. A monostatic (zero offset and common offset) 3D survey is already a time consuming task. An important fact which must be taken into account is the offset between the source and receiver antenna, because the distance between the antennas and the scattering objects is usually not large enough such that the offset between the source and receiver can be neglected.

FORWARD MODEL

For the multi-component 3-D imaging procedure we start with the expression of the scattered field using the Born approximation, which is given by

$$\hat{E}_k^s(\boldsymbol{x}^R,\omega) = \int_{\boldsymbol{x}^c\in\mathbb{D}^c} \hat{G}^{\mathrm{EJ}}_{k,r}(\boldsymbol{x}^R|\boldsymbol{x}^c,\omega)\chi_{r,s}(\boldsymbol{x}^c)\times \hat{G}^{\mathrm{EJ}}_{s,t}(\boldsymbol{x}^c|\boldsymbol{x}^S,\omega)\hat{J}^e_t(\boldsymbol{x}^S,\omega)\mathrm{d}V, \quad (1)$$

where $\mathbb{D}^c$ is the scattering domain and $\{k,r,s,t\} = \{1,2,3\}$. $\hat{G}^{\mathrm{EJ}}_{s,t}(\boldsymbol{x}^c|\boldsymbol{x}^S,\omega)$ describes the propagation of the vectorial electric field due to a point source $\hat{J}^e_t(\boldsymbol{x}^S,\omega)$ to the location of the contrast $\chi_{r,s}(\boldsymbol{x}^c)$ at position $\boldsymbol{x}^c$. This scatterer can be considered as a secondary source and the propagation from $\boldsymbol{x}^c$ towards the receiver is described by $\hat{G}^{\mathrm{EJ}}_{k,r}(\boldsymbol{x}^R|\boldsymbol{x}^c,\omega)$. The scattered electric field $\hat{E}^s_k(\boldsymbol{x}^R,\omega)$ is

measured at position $\boldsymbol{x}^R$, where $\{\boldsymbol{x}^S, \boldsymbol{x}^R\} \in \mathbb{D}^{SR}$. No direct waves nor multiples are assumed to be present in the data. We also assume that each point in the subsurface acts as an independent point scatterer producing only a singly reflected upward scattered signal. For an isotropic scatterer $\chi_{r,s}(\boldsymbol{x}^c)$ reduces to $\chi\delta_{r,s}(\boldsymbol{x}^c)$.
Taking into account the practical limitation of finite length source and receiver antennas; the fact that the orientation of the source and receiver is parallel to the interface, four different source-receiver combinations are possible. Eq. (1) reduces to

$$\hat{E}^s_\alpha(\boldsymbol{x}^R,\omega) = \int_{\boldsymbol{x}^c\in\mathbb{D}^c} \chi(\boldsymbol{x}^c)\hat{G}^{\mathrm{EJ}}_{\alpha,r}(\boldsymbol{x}^R|\boldsymbol{x}^c,\omega)\times \hat{G}^{\mathrm{EJ}}_{r,\beta}(\boldsymbol{x}^c|\boldsymbol{x}^S,\omega)\hat{J}^e_\beta(\boldsymbol{x}^S,\omega)\mathrm{d}V, \quad (2)$$

where $\{\alpha,\beta\} = \{1,2\}$ and $\{\boldsymbol{x}^S,\boldsymbol{x}^R\} \in \mathbb{D}^{SR}$, where $x_3^S = x_3^R = 0$. The configuration is depicted in Figure 1.

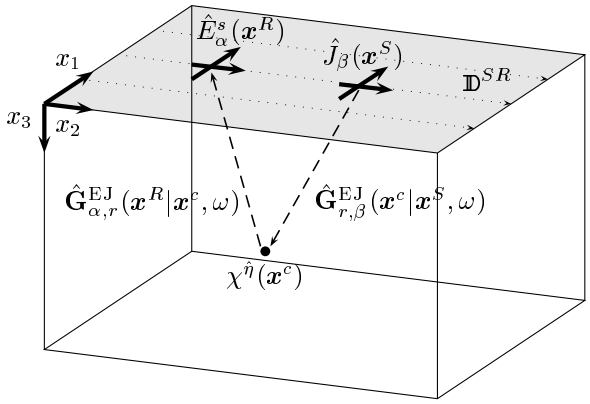

Figure 1. The configuration of the four possible source receiver setups.

Replace $\hat{J}_\beta(\boldsymbol{x}^S,\omega)$ by $\hat{S}(\omega)$, which indicates that we describe the finite length antennas with an effective point source approximation in Eq. (2). Eq. (2) is rewritten as a two-by-two matrix formulation for the scattered field due to a contrasting domain as

$$\hat{E}_{\alpha,\beta}(\boldsymbol{x}^R|\boldsymbol{x}^S,\omega) = \hat{S}(\omega)\int_{\boldsymbol{x}^c\in\mathbb{D}^c}\chi(\boldsymbol{x}^c)\hat{G}^{\mathrm{EJ}}_{\alpha,k}(\boldsymbol{x}^R|\boldsymbol{x}^c,\omega)\hat{G}^{\mathrm{EJ}}_{k,\beta}(\boldsymbol{x}^c|\boldsymbol{x}^S,\omega)\mathrm{d}V, \quad (3)$$

where $\hat{E}_{\alpha,\beta}$ describes the response of four possible source-receiver combinations due to an electric current source, where α and β indicates the orientation of the receiver and the source, respectively. Substitution of (de Hoop, 1995)

$$\hat{G}^{\mathrm{EJ}}_{k,r}(\boldsymbol{x}^c|\boldsymbol{x}^S,\omega) = \hat{G}^{\mathrm{EJ}}_{r,k}(\boldsymbol{x}^S|\boldsymbol{x}^c,\omega), \quad (4)$$

in Eq. (3) results in

$$\hat{E}_{\alpha,\beta}(\boldsymbol{x}^R|\boldsymbol{x}^S,\omega) = \hat{S}(\omega)\int_{\boldsymbol{x}^c\in\mathbb{D}^c}\chi(\boldsymbol{x}^c)\hat{G}^{\mathrm{EJ}}_{\alpha,k}(\boldsymbol{x}^R|\boldsymbol{x}^c,\omega)\hat{G}^{\mathrm{EJ}}_{\beta,k}(\boldsymbol{x}^S|\boldsymbol{x}^c,\omega)\mathrm{d}V. \quad (5)$$

WAVE FIELD EXTRAPOLATOR IN A HOMOGENEOUS SPACE

For a homogeneous space $\hat{G}^{\mathrm{EJ}}_{k,r}$ is given by (de Hoop, 1995)

$$\hat{G}^{\mathrm{EJ}}_{k,r}(\boldsymbol{x},\omega) = \hat{\eta}^{-1}[\partial_k\partial_r + k^2\delta_{k,r}]\hat{G}(R,\omega), \quad (6a)$$

$$\hat{G}(R,\omega) = \frac{\exp(-jkR)}{4\pi R}, \quad (6b)$$

$$R = |\boldsymbol{x}|, \quad (6c)$$

$$k = \frac{\omega}{c}. \quad (6d)$$

We assume that the source and receiver coordinates coincide (zero-offset), $\boldsymbol{x}^S = \boldsymbol{x}^R = \boldsymbol{x}^{ZO}$ and $x_3^{ZO} = 0$, which results in

$$\hat{E}^{ZO}_{\alpha,\beta}(\boldsymbol{x}^{ZO},\omega) = \hat{S}(\omega)\int_{\boldsymbol{x}^c\in\mathbb{D}^c}\chi(\boldsymbol{x}^c)\hat{G}^{\mathrm{EJ}}_{\alpha,k}(\boldsymbol{x}^{ZO}|\boldsymbol{x}^c,\omega)\hat{G}^{\mathrm{EJ}}_{\beta,k}(\boldsymbol{x}^{ZO}|\boldsymbol{x}^c,\omega)\mathrm{d}V. \quad (7)$$

The separate elements of the matrix in Eq. (7) are evaluated for the far field contributions. Eq. (7) can be written as

$$\hat{\mathbf{E}}^{ZO}(\boldsymbol{x}^{ZO},\omega) = \hat{S}(\omega)\int_{\boldsymbol{x}^c\in\mathbb{R}^c}\chi(\boldsymbol{x}^c)\hat{\mathbf{D}}_0(\boldsymbol{x}^{ZO}-\boldsymbol{x}^c,\omega)\mathrm{d}V, \quad (8)$$

where $\hat{\mathbf{E}}^{ZO}(\boldsymbol{x}^{ZO},\omega)$ consists of the elements $\hat{E}^{ZO}_{\alpha,\beta}(\boldsymbol{x}^{ZO},\omega)$ and $\hat{\mathbf{D}}_0(\boldsymbol{x},\omega)$ is the 3-D two-way wave field extrapolator for zero offset, which is given by

$$\hat{\mathbf{D}}_0(\boldsymbol{x},\omega) = \mathbf{f},\omega(\boldsymbol{x})\exp(-2jkR), \quad (9)$$

where

$$\mathbf{f}(\boldsymbol{x},\omega) = C\begin{bmatrix}(x_2^2+x_3^2)/R^2 & -x_1x_2/R^2,\\ -x_1x_2/R^2 & (x_1^2+x_3^2)/R^2\end{bmatrix}\frac{1}{R^2}, \quad (10a)$$

$$C = \frac{k^4}{\hat{\eta}^2(4\pi)^2}, \quad (10b)$$

where $\hat{\eta} = \sigma + j\omega\varepsilon$. The Greens functions, which describe the propagation of the electric field from the source to the contrasting domain and the propagation from the contrasting domain to the receiver, are combined in the 3-D two-way wave field extrapolator for each source-receiver orientation. Summarizing, this 3-D two-way wave field

extrapolator consists of an inner product of two vectorial Green's functions. For a homogeneous space and zero-offset this 3-D two-way wave field extrapolator contains simple elements when only the far field is taken into account.

INVERSE WAVE FIELD EXTRAPOLATOR IN A HOMOGENEOUS SPACE

The multi-component wave field extrapolator ($\hat{\mathbf{D}}_0$) describes the propagation of the vectorial electric field from the source to the isotropic point scatterer to the receiver. To obtain an image of the subsurface we must compensate for the propagation from the recording plane to another depth level inside the medium of investigation, or in other words, we have to find an approximate inverse of $\hat{\mathbf{D}}_0$. An exact inverse does not exist, so a stable approximate inverse $\hat{\mathbf{D}}_0^{inv}$ is derived in the spatial Fourier domain using the method of stationary phase. The two-dimensional spatial Fourier transform of $\hat{\mathbf{D}}_0$ is defined by

$$\tilde{\mathbf{D}}_0(k_1,k_2,x_3,\omega) = FFT\left\{\hat{\mathbf{D}}_0\right\}(k_1,k_2,x_3) = \int_{(x_1,x_2)\in\mathbb{R}^2} \hat{\mathbf{D}}_0(\boldsymbol{x},\omega)\exp[j(k_1x_1+k_2x_2)]\mathrm{d}A. \quad (11)$$

Next, the method of stationary phase for the evaluation of the two dimensional integral is used to obtain a useful expression in the spatial Fourier domain (see Felsen, 1973 and Bleistein, 1984). The expression for $\tilde{\mathbf{D}}_0(k_1,k_2,x_3,\omega)$ is obtained as

$$\tilde{\mathbf{D}}_0(k_1,k_2,x_3,\omega) = \frac{2\pi C}{(2k)^2}\begin{bmatrix}(k_2^2+k_3^2) & -k_1k_2\\ -k_1k_2 & (k_1^2+k_3^2)\end{bmatrix}\times \frac{\exp[-j(k_3|x_3|+\pi/2)]}{2k|x_3|}. \quad (12)$$

In the spatial Fourier domain, the inverse of the two-way forward 3D wave field extrapolator can be obtained by a simple inverse of the two-by-two matrix. The expression for $\tilde{\mathbf{D}}_0^{inv}$ is obtained as

$$\tilde{\mathbf{D}}_0^{inv}(k_1,k_2,x_3,\omega) = \frac{k|x_3|}{\pi C k_3^2}\begin{bmatrix}k_1^2+k_3^2 & k_1k_2\\ k_1k_2 & k_2^2+k_3^2\end{bmatrix} \exp[j(k_3|x_3|+\pi/2)]. \quad (13)$$

Note that for $\tilde{\mathbf{D}}_0^{inv}$ to be stable the evanescent waves must be suppressed and the vertical wavenumber, k_3 in Eq. (13), must satisfy (Berkhout, 1981)

$$k_3 = \sqrt{4k^2-k_1^2-k_2^2}, \qquad \text{for } k_1^2+k_2^2 \le 4k^2, \quad (14a)$$

$$= j\sqrt{k_1^2+k_2^2-4k^2}, \qquad \text{for } k_1^2+k_2^2 > 4k^2. \quad (14b)$$

The spatial equivalent of Eq. (13) can be recognized as

$$\hat{\mathbf{D}}_0^{inv} = \frac{4k^2}{4\pi^2 C}\begin{bmatrix}(x_1^2+x_3^2)/R^2 & x_1x_2/R^2\\ x_1x_2/R^2 & (x_2^2+x_3^2)/R^2\end{bmatrix}\exp(2jkR). \quad (15)$$

A simple relation between $\hat{\mathbf{D}}_0$ and $\hat{\mathbf{D}}_0^{inv}$ holds and is given by

$$\hat{\mathbf{D}}_0^{inv}(x_1,x_2,x_3,\omega) = -\frac{R^2k^2}{\pi^2C^2}\begin{bmatrix}0 & 1\\ -1 & 0\end{bmatrix}\hat{\mathbf{D}}_0^H(x_1,x_2,x_3,\omega)\begin{bmatrix}0 & 1\\ -1 & 0\end{bmatrix}. \quad (16)$$

A similar analysis can be carried out for single-component measurements. However, the obtained scalar inverse wave field extrapolator is not stable and will amplify the noise. On the other hand, the multi-component inverse wave field extrapolator, which uses four possible orientations of the source and receiver antennas, is stable. Note that $\tilde{\mathbf{D}}_0^{inv}$ is the exact inverse of $\tilde{\mathbf{D}}_0$ for propagating waves, whereas it suppresses evanescent waves.

INVERSE OF WAVE FIELD EXTRAPOLATOR IN TWO HOMOGENEOUS HALFSPACES

Due to the fact that the expressions of the forward two-way wave field extrapolator were quite simple in a homogeneous space an analytical analysis was possible. However, for a homogeneous halfspace an analytical approach is not feasible. A numerical implementation to determine the approximate inverse is still possible. An important benefit is that also the offset between source and receiver can be taken into account. We introduce the wave field operator $\hat{\mathbf{D}}_h(\boldsymbol{x}-\boldsymbol{x}^M)$, which takes into account the offset between the source and receiver for a specific offset and orientation, where $\boldsymbol{x}^M$ is the midpoint between the source and receiver antenna. To determine the inverse operator we use the far field expressions (see also Engheta and Papas, 1982) in Cartesian coordinates. The inner product of the two Greens functions (See Eq. (5)) must be determined for each source-receiver position. Then a two-dimensional spatial FFT must be carried out. For each k_1, k_2 combination an inverse matrix can be numerically determined, which results in a representation of the imaging operator in the spatial Fourier domain. Note that for $\hat{\mathbf{D}}_h^{inv}(\boldsymbol{x}-\boldsymbol{x}^M)$ to be stable Eqs. (14a) and (14b) must again be satisfied.

IMAGING PRINCIPLE

The approximate inverse of the two-way wave field extrapolator $\hat{\mathbf{D}}_h^{inv}$ compensates for all travel times and amplitudes involved in the specific subsurface layer, including radiation characteristics of the (point) source and

(point) receiver. Applying this operator on the measured data we obtain for a specific depth level x_3^n,

$$\langle \hat{\chi}(\boldsymbol{x}^n,\omega)\mathbf{I}\rangle = \int_{\boldsymbol{x}^M\in\mathbb{D}^{ZO}} \frac{\hat{\mathbf{D}}_h^{inv}(\boldsymbol{x}^n-\boldsymbol{x}^M)}{\hat{S}(\omega)}\hat{\mathbf{E}}^M(\boldsymbol{x}^M)\mathrm{d}A, \quad (17)$$

where $\hat{\mathbf{E}}^M(\boldsymbol{x}^M)$ is the measured electric field using a common offset configuration and $\boldsymbol{x}^n = (x_1, x_2, x_3^n)$. The actual wave field extrapolation procedure can be applied as a two-dimensional convolution procedure in the space domain. However, the wave field extrapolation is most convenient carried out in the spatial Fourier domain, caused by the low computation time compared with a convolution.

Next, the imaging principle is applied, which formulates that the data at zero traveltime of the inverse extrapolated recordings relate to the contrast of the medium of investigation (Berkhout, 1981).

As a consequence we simply add the result for all (positive and negative) frequencies to obtain the imaged contrast in space domain which can be written as

$$\langle \chi(\boldsymbol{x}^n)\mathbf{I}\rangle = \frac{1}{N_\omega}\sum_\omega \langle \hat{\chi}(\boldsymbol{x}^n,\omega)\mathbf{I}\rangle. \quad (18)$$

Note that for a zero offset measurement $\hat{\mathbf{D}}_h^{inv}(\boldsymbol{x}^n-\boldsymbol{x}^M)$ is replaced by $\hat{\mathbf{D}}_0^{inv}(\boldsymbol{x}^n-\boldsymbol{x}^{ZO})$.

SYNTHETIC IMAGING RESULTS

The spatial resolution of a single point diffractor is investigated. Therefore, full 3D downward extrapolation of the measured electric field to the depth level of the diffractor is carried out. For the special situation of one diffraction point only, with unit amplitude, according to

$$\chi(\boldsymbol{x}^n) = \delta(\boldsymbol{x}^n-\boldsymbol{x}^c), \quad (19)$$

the measured electric field may be expressed in terms of the source function $\hat{S}(\omega)$. In the following we consider for convenience a source function with unit amplitude. The full 3D downward extrapolation of sources and detectors to the diffractor depth level $x_3^n = x_3^c$ results in the resolution function

$$< \hat{\chi}(x_1,x_2,x_3^n)\mathbf{I} > = \frac{k}{\pi}\frac{J_1(2kr)}{r}\mathbf{I}, \quad (20)$$

where J_1 is the first order Bessel function and $r = \sqrt{(x_1)^2+(x_2)^2}$. This result, which is depicted in Figure 2, represents the (monochromatic) zero-offset response of the diffractor, 'measured' at the depth level of the diffractor x_3^n. Instead of a spatial delta function we observe a circular symmetric resolution function. The limited resolution is due to the suppression of the evanescent field (Berkhout, 1984). The result for the multi-component imaging is a circular symmetric resolution function, while other imaging schemes show no longer a circular and symmetric resolution function (not shown).

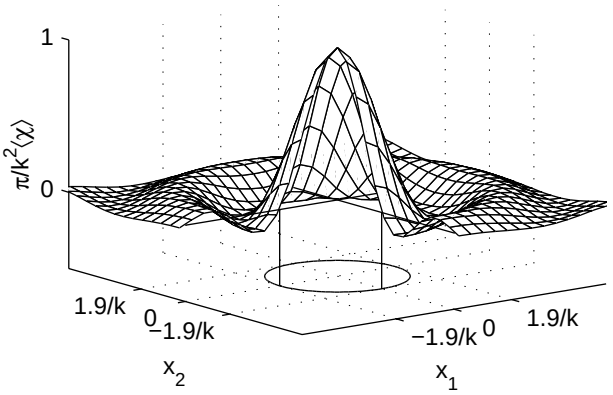

Figure 2. Spatial resolution for a point diffractor

EXPERIMENTAL RESULTS

At a test location several objects were buried in sand. Measurements were made with the 900 MHz pulseEKKO system using different polarisations of the source and receiver antennas. The spatial sampling is 5 cm inline and crossline and the offset between the source and receiver antennas was 30 cm to enable multi-component measurements. Prior to the imaging the time zero was adjusted and the average trace was removed from the data, because the imaging scheme uses only reflected waves and not direct waves. The data was imaged using a relative permittivity of $\varepsilon_r = 3.1$ and was imaged taking into account the radiation patterns in a homogeneous halfspace and the offset between the source and receiver. The source wavelet is not taken into account. The results are obtained using a combination of the source oriented in the x_1-direction and the receiver oriented in the x_1- and x_2-direction. Surfaces of constant absolute value are plotted in Figures 3, 4 and 5 for different observation angles.

The spatial sampling of the imaging domain is 5 cm in the horizontal and vertical directions. Several objects are present at the test site. Objects A, B and C are steel pipes. The length of pipes A and B is 1 meter. Objects A and B are horizontal pipes and object C is a dipping pipe. Objects D and E are metal spheres and object F is a plastic sphere. Pipes A and B have the largest amplitude and the plastic sphere has the smallest amplitude. Some other anomalies are present, which have amplitudes comparable with the amplitude of the imaged

plastic sphere. Note that due to inaccurate lateral positioning in the x_2-direction the images of the pipes are not completely straight.

CONCLUSIONS

A multi-component electromagnetic image reconstruction technique has been derived, which is based on the vectorial wave equation. For a homogeneous space an analytical analysis has been carried out. The result for the multi-component imaging of a point scatterer in a homogeneous space is a circular symmetric resolution function, while other imaging schemes show no longer a circular and symmetric resolution function, which is an indication that the radiation characteristics of the source and receiver still influence the obtained image for conventional scalar imaging schemes.
For two homogeneous halfspaces it is not feasible to carry out a similar analytical approach. However, in numerical sense the same procedure can be carried out, which has the important benefit that also the offset between the source and receiver can be taken into account.
Experimental results of the multi-component 3D vectorial electromagnetic imaging scheme have been presented. The radiation patterns on a homogeneous halfspace and the offset between the source and receiver have been taken into account and several objects were correctly imaged.

ACKNOWLEDGEMENTS

This research is supported by the Dutch Technology Foundation (STW).

REFERENCES

Berkhout, A.J., 1981, Wave field extrapolation in seismic migration, a tutorial, *Geophysics*, Vol. 46 No. 12, pp. 1638-1656.

Berkhout, A.J., 1984, Handbook of geophysical exploration, Section 1. Seismic exploration Vol. 12 Seismic resolution, a quantitative analysis of resolving power of acoustical echo techniques, Geophysical press, London.

Bleistein, N., 1984, Mathematical methods for wave phenomena, Academic Press, London.

Engheta, N. and Papas, C.H., 1982, Radiation patterns of interfacial dipole antennas, *Radio Science*, Vol. 17, No. 6, pp. 1557-1566.

Felsen, L.B., 1973, Radiation and scattering of waves, Prentice-Hall, Englewood Cliffs, N.J.

Fisher, E., McMechan, G.A., Annan, A.P. and Cosway, S.W., 1992, Examples of reverse-time migration of single-channel, ground-penetrating radar profiles, *Geophysics*, Vol. 57, No. 4, pp. 577-586.

de Hoop, A.T., 1995, Handbook of Radiation and Scattering of Waves, Academic Press, Amsterdam.

Johansson, E.M., Mast, J.E., 1994, Three-dimensional ground penetrating radar imaging using synthetic aperture time-domain focusing, *SPIE*, Vol. 2275, pp. 205-214.

Mast, J.E. and Johansson, E.M., 1994, Three-dimensional ground penetrating radar imaging using multi-frequency diffraction tomography, *SPIE* Vol. 2275, pp. 196-203.

Moran, M.L., Arcone, S.A., Delaney, A.J., 1998, *Seventh international conference on Ground Penetrating Radar*, Lawrence, Kansas, USA, May 27-30 1998, pp. 225-231.

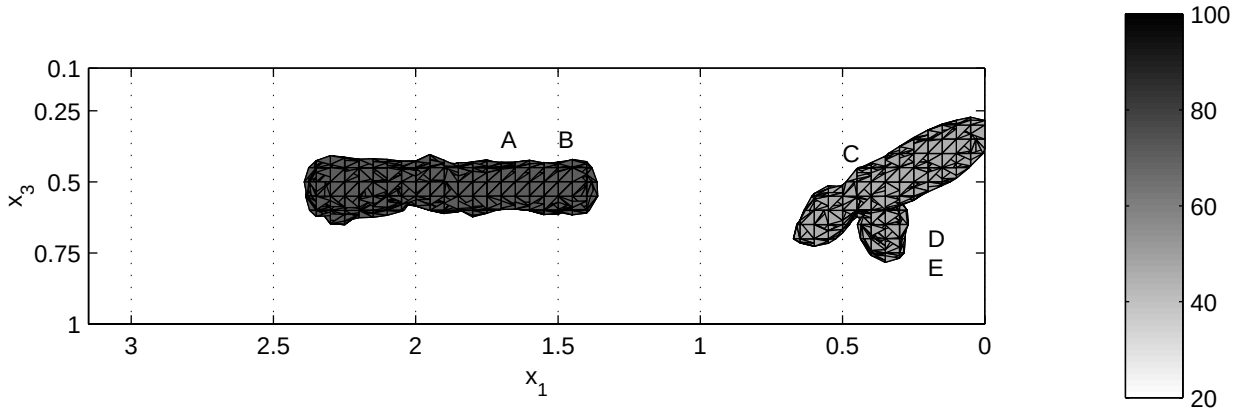

Figure 3. Sideview of the multi-component imaging results using pE 900 MHz antennas.

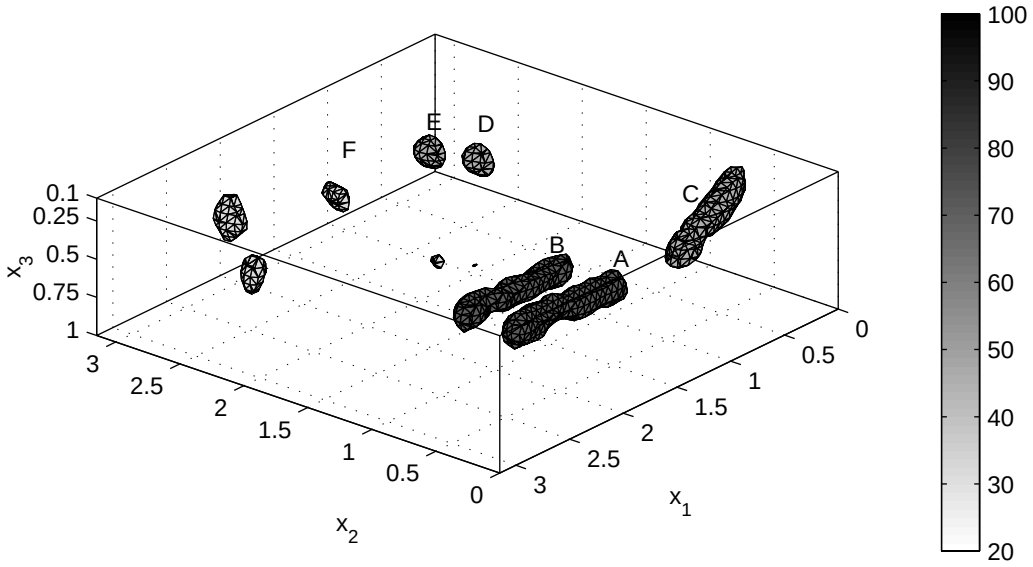

Figure 4. Multi-component imaging results using pE 900 MHz antennas.

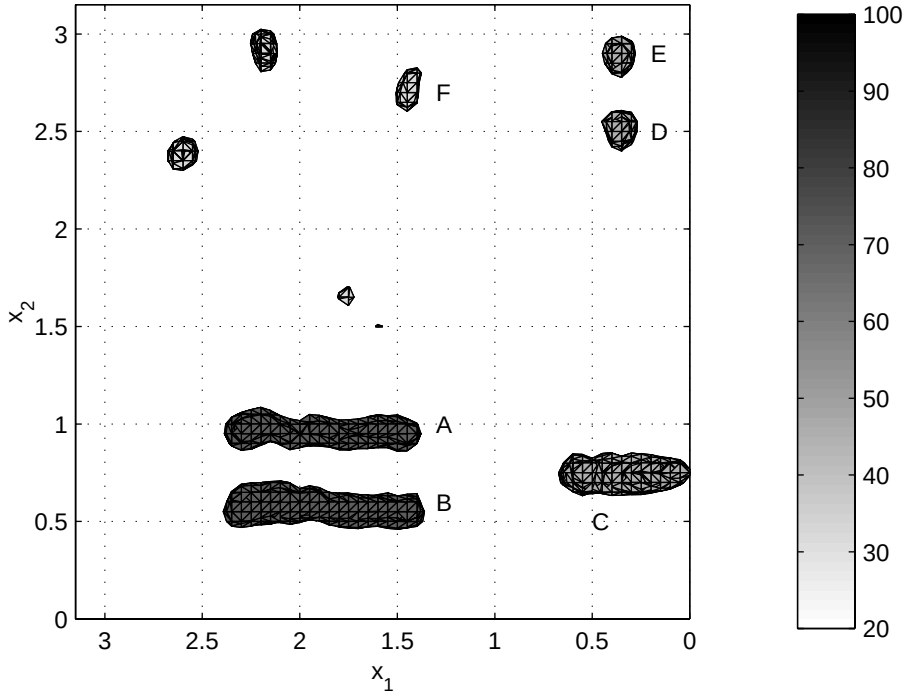

Figure 5. Topview of the multi-component imaging results using pE 900 MHz antennas.